Force and power of flapping plates in a fluid

Gao-Jin Li and Xi-Yun Lu

Journal of Fluid Mechanics / Volume 712 / December 2012, pp 598 - 613
DOI: 10.1017/jfm.2012.443, Published online: 09 October 2012

J. Fluid Mech. (2012), *vol.* 712, *pp.* 598–613. © Cambridge University Press 2012
doi:10.1017/jfm.2012.443

Force and power of flapping plates in a fluid

Gao-Jin Li and Xi-Yun Lu†

Department of Modern Mechanics, University of Science and Technology of China, Hefei, Anhui 230026, China

(Received 14 August 2012; revised 14 August 2012; accepted 6 September 2012; first published online 9 October 2012)

The force and power of flapping plates are studied by vortex dynamic analysis. Based on the dynamic analysis of the numerical results of viscous flow past three-dimensional flapping plates, it is found that the force and power are strongly dominated by the vortical structures close to the body. Further, the dynamics of the flapping plate is investigated in terms of viscous vortex-ring model. It is revealed that the model can reasonably reflect the essential properties of the ring-like vortical structure in the wake, and the energy of the plate transferred to the flow for the formation of each vortical structure possesses a certain relation. Moreover, simplified formulae for the thrust and efficiency are proposed and verified to be reliable by the numerical solutions and experimental measurements of animal locomotion. The results obtained in this study provide physical insight into the understanding of the dynamic mechanisms relevant to flapping locomotion.

Key words: biological fluid dynamics, propulsion, vortex dynamics

1. Introduction

The flapping plate is usually applied to mimic the wing or fin motion of flying or swimming animals for locomotion through a fluid. Some experiments and numerical simulations on the three-dimensional (3D) flapping plate or foil have been performed (e.g. von Ellenrieder, Parker & Soria 2003; Blondeaux *et al.* 2005; Dong, Mittal & Najjar 2006; Narasimhan *et al.* 2006; Buchholz & Smits 2008) and illustrated that ring-like vortical structures are formed in the wake. Dabiri (2009) has highlighted that the principles of vortex-ring formation possess intrinsic connections with biological locomotion. On the other hand, extensive studies have revealed that the wake relevant to animal locomotion demonstrates obvious ring-like vortical structures, such as separate rings in insects and birds flying slowly or hovering (e.g. Willmott, Ellington & Thomas 1997; Altshuler *et al.* 2009) and fish swimming (e.g. Müller *et al.* 1997; Drucker & Lauder 1999; Nauen & Lauder 2002), and connected rings in birds and bats flying relatively fast (e.g. Hedenström, Rosén & Spedding 2006; Hedenström *et al.* 2007). Based on the observations, inviscid vortex-ring models have been employed to analyse the relevant dynamics (e.g. Müller *et al.* 1997; Nauen & Lauder 2002; Wang & Wu 2010), while the viscous effect, which plays an important role in the generation and evolution of vortices, is scarcely considered in the previous analyses.

† Email address for correspondence: xlu@ustc.edu.cn

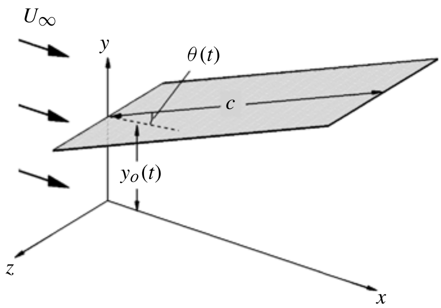

FIGURE 1. Schematic of the flapping plate.

There have been a variety of vorticity dynamic theories that have shed light on some aspects of vortex dynamics. Wu (1981) proposed the vorticity moment theory, which provided the relationship between forces and the rate of change of vorticity moments in viscous flow. Chang (1992) developed a diagnostic force theory to separate potential forces such as added mass and inertial forces and to distinguish the contributions of individual fluid elements to forces. Wu, Ma & Zhou (2006) and Wu, Lu & Zhuang (2007) derived some unconventional force expressions based on derivative-moment transformations. These transformations are used to replace the original integrand by the moments of its spatial derivatives, which, if necessary, can be represented by other terms in the differential motion equations to explicitly reveal the effect of various local dynamic processes and structures on the integrated performance. Then, these theories have been successfully applied in analysing the local dynamic processes of bluff-body flows (e.g. Wu *et al.* 2007; Xu, Chen & Lu 2010) and insect flight (e.g. Hsieh, Chang & Chu 2009; Hsieh *et al.* 2010; Wang & Wu 2010). It should be noted that all these studies have only dealt with the force; however, the power, which is related to the energy and further to the efficiency, has been relatively less studied.

In the present study, the force and power of the flapping plates and their connections with the local dynamic processes and vortical structures will be investigated. The purpose of this study is to achieve an improved understanding of some of the fundamental mechanisms relevant to the dynamics of a flapping plate.

This paper is organized as follows. The physical problem and the numerical method with its validation are described in § 2. The force and power expressions in terms of local flow structures are given in § 3. The force and power linked to the local vortical structures are discussed in § 4. The dynamics of the flapping plate is further analysed in terms of the viscous vortex-ring model in § 5. Finally, concluding remarks are made in § 6.

2. Physical problem and numerical method

2.1. *Problem statement*

The 3D flapping plate in a uniform flow is considered. Figure 1 shows the schematic of the flapping plate and the coordinate system (x, y, z) with the x-axis along the streamwise direction, the y-axis along the vertical direction and the z-axis along the spanwise direction of the plate. The plate heaves in the vertical direction and pitches around its leading edge along the spanwise direction of the plate. The heaving and

Case	Plate	A	St	Re
1	I	0.5	0.6	500
2	II	0.5	0.6	500
3	III	0.5	0.6	500
4	IV	1.0	0.6	500
5	I	0.5	0.4	500
6	I	0.5	0.8	500
7	I	0.5	0.6	100
8	I	0.5	0.6	200
9	I	0.5	0.6	1000

Plate	Shape
I	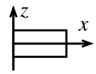
II	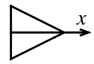
III	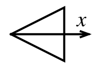
IV	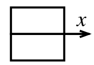

TABLE 1. Parameters and plate shapes in the simulation.

pitching motions are described as

$$y_o(t) = A_y \cos(2\pi f t), \tag{2.1a}$$
$$\theta(t) = A_\theta \sin(2\pi f t), \tag{2.1b}$$

where A_y and A_θ represent the heaving and pitching amplitudes, respectively, f denotes the flapping frequency and t is time.

The incompressible Navier–Stokes equations are used to describe the flow dynamics of the flapping plate, which are normalized by the incoming uniform flow speed U_∞ and the chord length of the plate c as indicated in figure 1. To solve the equations, the initial and boundary conditions are given as follows. A uniform flow is used as an initial condition. No-slip and no-penetration velocity boundary conditions are applied on the surface of the plate. A uniform velocity is set at the upstream far boundary and a Neumann velocity boundary condition $\partial \boldsymbol{u}/\partial n_F = 0$ is employed along the side boundaries of the computational domain, where $\boldsymbol{n}_F$ indicates the unit vector in the boundary normal direction. The downstream far boundary condition $\partial \boldsymbol{u}/\partial t + U_\infty \partial \boldsymbol{u}/\partial x = 0$ is specified.

Without loss of generality, as listed in table 1, four plate shapes with area $A = 0.5$ and 1 are considered. The corresponding aspect ratio, defined by $AR = s_m^2/A$ with s_m being the maximal span length of the plate, lies in the range of 0.5–2 for the plates, consistent with the morphological parameters for fish caudal fins, such as $AR \simeq 0.6$ of sand goby (*Pomatochistus minutus*) (Withers 1981), and for bird wings, such as $AR \simeq 1.9$ of woodcock (*Philohela minor*) (Sambilay 1990). Motivated by the measurements of animal locomotion (e.g. Richard 1958; Ellington 1984*a*,*b*; Taylor, Nudds & Thomas 2003) as well as the model-based experiments (e.g. von Ellenrieder *et al.* 2003; Buchholz & Smits 2008) and numerical simulations (e.g. Blondeaux *et al.* 2005; Dong *et al.* 2006), the governing parameters are chosen as follows: heaving amplitude $A_y/c = 0.5$, pitching amplitude $A_\theta = \pi/6$, Strouhal number $St = 2A_y f/U_\infty = 0.4$, 0.6 and 0.8, and flapping Reynolds number $Re = U_\infty c/\nu = 100$, 200, 500 and 1000, where ν is the kinematic viscosity. As the effect of turbulence

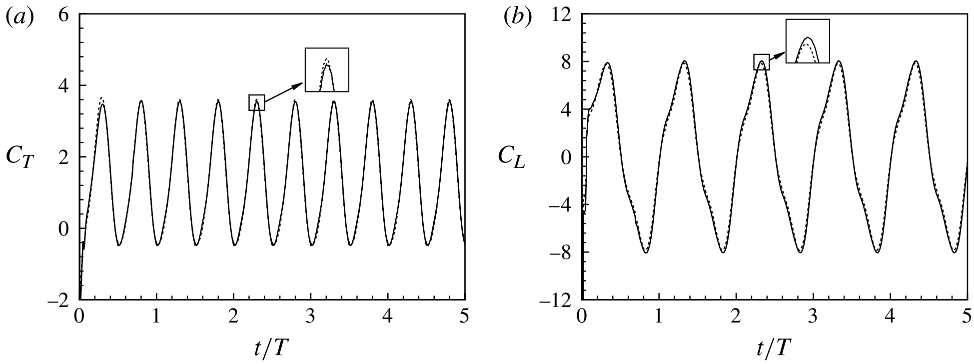

FIGURE 2. Time-dependent (*a*) thrust coefficient C_T and (*b*) lift coefficient C_L calculated under different computational conditions for $A = 0.5$, $Re = 500$ and $St = 0.6$. Solid line: finest lattice spacing $\Delta x = c/160$, time step $\Delta t = T/6400$ and computational domain $[-12, 12] \times [-10, 10] \times [-10, 10]$. Dashed line: $\Delta x = c/80$, $\Delta t = T/3200$ and computational domain $[-9, 9] \times [-8, 8] \times [-8, 8]$.

should be negligibly weak even for the largest Reynolds number considered here, the fluid flow is assumed to be laminar flow.

2.2. *Numerical method and validation*

In this study, a multi-block immersed boundary–lattice Boltzmann method (IB-LBM) is used to solve the equations. The lattice Boltzmann method (LBM) provides an alternative method for solving viscous fluid flows. Based on the mesoscopic kinetic models, the algorithm of the LBM, which avoids solving the Poisson equation, is extremely simple compared with the conventional numerical schemes. The relevant advantages include high computational efficiency and low numerical dissipation (Chen & Doolen 1998). Here, a multi-block LBM technique (Filippova & Hänel 1998; Yu, Mei & Shyy 2002) is employed to solve our problem. On the other hand, the immersed boundary (IB) method, which treats the solid boundary by adding a boundary force to the momentum equation, has been widely applied for moving bodies (Goldstein, Handler & Sirovich 1993; Peskin 2002). The IB technique combined with the LBM has also been widely applied to simulate solid–fluid interaction problems (e.g. Feng & Michaelides 2004; Shi & Lim 2007; Gao & Lu 2008). Moreover, a detailed description of the numerical method and the relevant validation have been given in our previous papers (e.g. Gao & Lu 2008; Zhang, Liu & Lu 2010; Li, Zhu & Lu 2012).

To validate the method, convergence checks have been carried out to assess the effect of grid resolution and domain size. As a typical case, we calculated the flapping plate of $A = 0.5$ at $Re = 500$ and $St = 0.6$ (i.e. case 1 in table 1) for different lattice spacings and different sizes of the computational domain. The time-dependent thrust and lift coefficients are shown in figure 2. The results from the two different computations agree well with each other. It is confirmed that the computed results are independent of the lattice spacing and computational domain size. The results given below have been calculated on the finer grid and the larger domain. The computational domain is thus chosen as $[-12, 12] \times [-10, 10] \times [-10, 10]$ in the streamwise (x), vertical (y) and spanwise (z) directions, with the finest lattice spacing of $c/160$ in the region of the plate and the coarsest spacing of $c/40$ in the far-field region near the

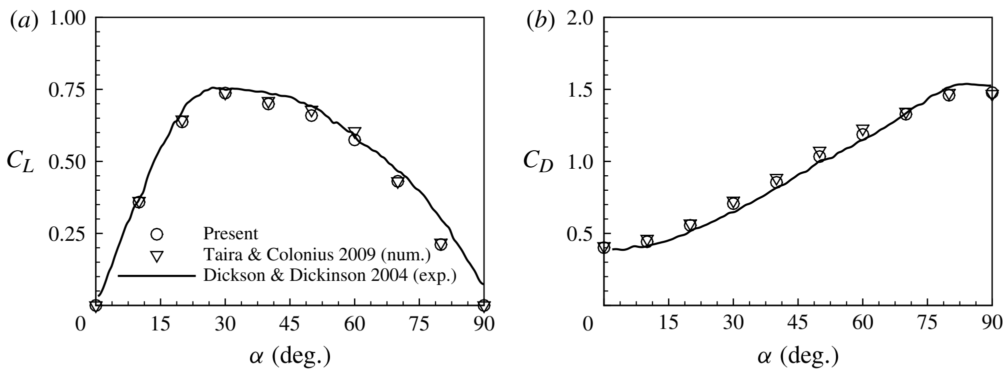

FIGURE 3. Comparison of the present result and previous data obtained experimentally (Dickson & Dickinson 2004) and numerically (Taira & Colonius 2009) for a rectangular plate with $AR = 2$ at $Re = 100$.

boundaries. The time step is $\Delta t = T/6400$, with T being the flapping period. All the cases have been calculated over 10 flapping cycles in our simulation to ensure that the flow has reached a stationary state.

To perform quantitative comparison with previous experimental data and numerical results, we first consider a rectangular plate being impulsively translated in a viscous fluid, which has been studied experimentally (Dickson & Dickinson 2004) and numerically (Taira & Colonius 2009). Figure 3 shows the lift C_L and drag C_D coefficients versus the angle of attack α for the plate with an aspect ratio $AR = 2$ at $Re = 100$. It is seen that our calculated results are in good agreement with the previous experimental and numerical data.

To validate the simulation of a 3D moving body, we have calculated viscous flow around a pair of robotic fruit fly wings, which was experimentally studied by Dickinson *et al.* (1999). This case has also been employed by Dai *et al.* (2012) for their code validation, and the relevant parameters are described as follows: Reynolds number $Re = U\bar{c}/\nu = 164$ with $\bar{c}$ being the average chord and U the average translational velocity at the wing tip, wing span $s = 2.84\bar{c}$, wing area $A = 2.16\bar{c}^2$ and flapping frequency $f = 0.059U/\bar{c}$. The flapping cycle is composed of two translational phases, in which the wings sweep with a high angle of attack, and two rotational phases, in which the wings rotate symmetrically with respect to the stroke reversal, and lasts 16 % of the flapping period. The stroke amplitude is 160° and the angle of attack at mid-stroke is 40°. Figure 4 shows the time-dependent lift coefficient from the fourth cycle. It is identified that our result agrees well with the previous numerical result and is reasonably consistent with the experimental data.

3. Dynamic expressions in terms of local flow structures

To analyse the dynamic expressions conveniently, the coordinate system is chosen to be fixed with the fluid at infinity (Wu *et al.* 2006, 2007), so that the plate moves with a velocity $-\boldsymbol{U} = [-U_\infty, 0, 0]$ in the quiescent fluid. Let V_f be a 3D incompressible fluid domain, surrounding a solid body V_B and bounded externally by an arbitrary control surface Σ. The force $\boldsymbol{F}$ on the solid body V_B and the power P that is

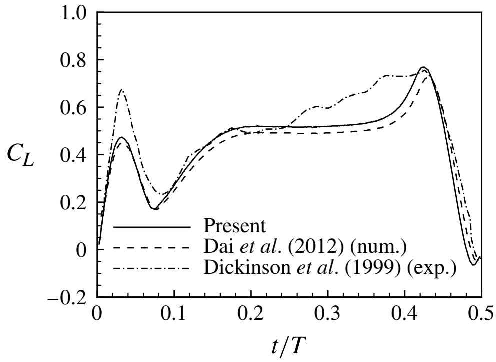

FIGURE 4. Time-dependent lift coefficient during one flapping cycle for a robotic fly model and a comparison with the results obtained experimentally (Dickinson, Lehmann & Sane 1999) and numerically (Dai, Luo & Doyle 2012).

transferred from the body to the flow are expressed as

$$\boldsymbol{F}(t) = -\int_{\partial B} \boldsymbol{t}\,\mathrm{d}S, \quad P(t) = \int_{\partial B} \boldsymbol{t}\cdot\boldsymbol{u}_B\,\mathrm{d}S, \tag{3.1}$$

where $\boldsymbol{u}_B$ is the velocity of the body surface and $\boldsymbol{t} = -p\boldsymbol{n} + \boldsymbol{\tau} + \boldsymbol{\tau}_s$ is the surface stress, with $\boldsymbol{n}$ being the outward normal vector on the body surface ∂B and Σ. Here, p is the pressure, $\boldsymbol{\tau} = \mu\boldsymbol{\omega}\times\boldsymbol{n}$ is the viscous force, and $\boldsymbol{\tau}_s = 2\mu[(\boldsymbol{n}\times\nabla)\times\boldsymbol{u}]$ represents the viscous force due to motion and deformation of the surface, with μ being the fluid viscosity. The integral of $\boldsymbol{\tau}_s$ on ∂B identically vanishes for $\boldsymbol{F}$ and is not necessarily zero for P, even though it is usually small.

For the flapping plate considered here, the input power due to the heaving and pitching motions, i.e. $\boldsymbol{u}_o(t) = (0, \dot{y}_o, 0)$ and $\boldsymbol{\Omega}(t) = (0, 0, \dot{\theta})$, where the dot denotes the time derivative, is given by

$$P_{in}(t) = \int_{\partial B} [\boldsymbol{t}\cdot\boldsymbol{u}_o(t) + (\boldsymbol{r}\times\boldsymbol{t})\cdot\boldsymbol{\Omega}(t)]\,\mathrm{d}S. \tag{3.2}$$

Combining (3.1) with the velocity condition $\boldsymbol{u}_B = -\boldsymbol{U} + \boldsymbol{u}_o(t) + \boldsymbol{\Omega}(t)\times\boldsymbol{r}$ on the solid body, the input power can further be represented as

$$P_{in}(t) = -\boldsymbol{F}(t)\cdot\boldsymbol{U} + P(t), \tag{3.3}$$

which means that the total input power is composed of the power of the plate forward motion and the power transferred to the flow. Using the derivative moment transformations (Wu *et al.* 2006, 2007), $\boldsymbol{F}$ and P can be expressed as

$$\boldsymbol{F} = -\frac{\mathrm{d}\boldsymbol{I}}{\mathrm{d}t} - \boldsymbol{F}_l - \boldsymbol{F}_B - \boldsymbol{F}_\Sigma, \tag{3.4a}$$

$$P = \frac{\mathrm{d}K}{\mathrm{d}t} + P_B + \Phi + P_\Sigma, \tag{3.4b}$$

where

$$\boldsymbol{I} = \frac{\rho}{2}\int_V \boldsymbol{x}\times\boldsymbol{\omega}\,\mathrm{d}V, \quad \boldsymbol{F}_l = \rho\int_V \boldsymbol{l}\,\mathrm{d}V, \quad \boldsymbol{F}_B = -\rho\frac{\mathrm{d}}{\mathrm{d}t}\int_{V_B} \boldsymbol{u}\,\mathrm{d}V, \tag{3.5a}$$

$$\left.\begin{aligned} K &= \rho \int_V \boldsymbol{x}\cdot\boldsymbol{l}\,\mathrm{d}V, \quad P_B = -\frac{\rho}{2}\frac{\mathrm{d}}{\mathrm{d}t}\int_{V_B}\boldsymbol{u}\cdot\boldsymbol{u}\,\mathrm{d}V, \\ \varPhi &= \mu \int_{V_f} (\boldsymbol{\omega}\cdot\boldsymbol{\omega} + 2\nabla\cdot[(\boldsymbol{u}\cdot\nabla)\boldsymbol{u}])\,\mathrm{d}V. \end{aligned}\right\} \tag{3.5b}$$

Here, $V = V_f + V_B$ denotes an analysis domain and has an external boundary Σ; $\boldsymbol{I}$ and K represent the vortical impulse and the kinetic energy, with ρ being the fluid density; $\boldsymbol{l} = \boldsymbol{\omega} \times \boldsymbol{u}$ is the Lamb vector; and $\boldsymbol{F}_l$ is the vortex force (Wu *et al.* 2006). The terms with the subscript B correspond to the part replaced by the solid body V_B. The two parts in the integral of $\varPhi$ respectively denote the dissipation caused by the enstrophy, which is directly related to the reduction of the kinetic energy, and the dissipation related to $\boldsymbol{\tau}_s$, which does not influence the change of kinetic energy but always directly dissipates into heat (Wu *et al.* 2006). Finally, $\boldsymbol{F}_\Sigma$ and P_Σ are the relevant surface integrals on Σ, i.e.

$$\boldsymbol{F}_\Sigma = \frac{\rho}{2}\int_\Sigma \left(\boldsymbol{n}\times\frac{\partial\boldsymbol{u}}{\partial t}\right)\times\boldsymbol{x}\,\mathrm{d}S - \frac{\rho}{2}\int_\Sigma (\boldsymbol{u}_\Sigma\cdot\boldsymbol{n})(\boldsymbol{x}\times\boldsymbol{\omega})\,\mathrm{d}S - \int_\Sigma (-p_0\boldsymbol{n}+\boldsymbol{\tau})\,\mathrm{d}S, \tag{3.6a}$$

$$\begin{aligned} P_\Sigma = \rho \int_\Sigma &\left[\frac{1}{2}(\boldsymbol{n}\cdot\boldsymbol{x})\frac{\partial}{\partial t}(\boldsymbol{u}\cdot\boldsymbol{u}) - \frac{\partial}{\partial t}[(\boldsymbol{x}\cdot\boldsymbol{u})\boldsymbol{u}]\cdot\boldsymbol{n}\right]\mathrm{d}S \\ &- \rho\int_\Sigma (\boldsymbol{u}_\Sigma\cdot\boldsymbol{n})[\boldsymbol{x}\cdot(\boldsymbol{\omega}\times\boldsymbol{u})]\,\mathrm{d}S - \int_\Sigma (-p_0\boldsymbol{n}+\boldsymbol{\tau}+\boldsymbol{\tau}_s)\cdot\boldsymbol{u}\,\mathrm{d}S, \end{aligned} \tag{3.6b}$$

where p_0 is the total pressure and $\boldsymbol{u}_\Sigma$ is the velocity relative to the control surface Σ. When Σ retreats to infinity, the surface integrals on Σ (i.e. $\boldsymbol{F}_\Sigma$ and P_Σ) and $\boldsymbol{F}_l$ in (3.4) vanish. Then, the force expression (3.4*a*) will recover the vorticity moment theory (Wu 1981).

4. Force and power linked to the local vortical structures

The expressions (3.4) are applied to analyse the results of flapping plates for the cases listed in table 1. For all the cases, two isolated ring-like vortical structures are formed during each flapping cycle, and the wake is mainly composed of two sets of vortical structures. For clarity, we here use case 1 as a basic case to perform detailed analysis.

Figure 5(*a*) shows the 3D perspective view of the vortical structures exhibited by an isosurface of the Q criterion (Hunt, Wray & Moin 1988), described as $Q = -(\|\boldsymbol{S}\|^2 - \|\boldsymbol{\Omega}\|^2)/2$, where $\boldsymbol{S}$ and $\boldsymbol{\Omega}$ denote the strain and the rotation tensor, respectively. A positive value of Q represents the regions in which the rotation exceeds the strain. Thus, the instantaneous vortical structures depicted by $Q = 2$ are illustrated in figure 5(*a*). The relevant wake topology of flapping foils has been well discussed by Dong *et al.* (2006). To examine the influence of the plate shape on the vortical structures, figure 5(*b*) also shows the 3D vortical structures for case 2 (i.e. plate II) in table 1. It is seen that the ring-like vortical structures are formed in the wake of the flapping plates with some differences in small-scale structures for both cases. The plate shape does not affect the essential feature of the wake topology, which is consistent with the previous finding (Dong *et al.* 2006).

From the side view of case 1 in figure 5(*c*), the vorticity magnitude surface is shown to capture the vorticity distribution, and the isosurface of the Q criterion is used to highlight the vortex cores. Moreover, the wake is artificially divided into sub-regions to distinguish the local vortical structures from $R1$ to $R8$ (or Ri, $i = 1, 2, \ldots, 8$).

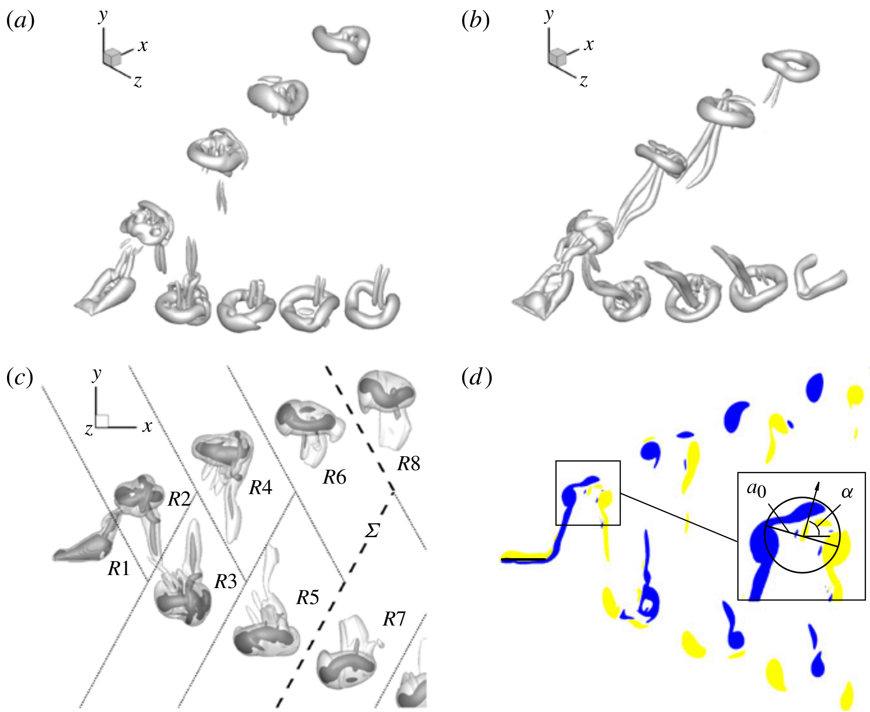

FIGURE 5. (Colour online) Instantaneous vortical structures at $t/T = 10.5$ with the plate reaching the lowest point of the heaving motion. (*a*,*b*) Perspective view of the 3D vortical structures visualized by Q criterion with $Q = 2$ for case 1 (plate I) and case 2 (plate II), respectively. (*c*) Side view of the isosurfaces of vorticity magnitude $\|\boldsymbol{\omega}\| = 1$ exhibited by light grey and of $Q = 2$ by dark grey for case 1. The wake is divided into sub-regions to distinguish the local vortical structures from $R1$ to $R8$ (or Ri, $i = 1, 2, \ldots, 8$). The borders are chosen to avoid cutting any distinct vortices and move with the structures during the flow evolution. (*d*) Spanwise vorticity distribution on the spanwise symmetric plane for case 1. The vorticity distribution of $R2$, which is used to measure the parameters of the equivalent vortex ring, is enlarged in the inset.

The borders are chosen to avoid cutting any distinct vortices and move with the structures during the flow evolution. The corresponding spanwise vorticity contour in the spanwise symmetry plane is shown in figure 5(*d*), which will be used to measure the equivalent vortex-ring properties of the ring-like vortical structure.

Figure 6(*a*) shows the time-dependent thrust coefficient $C_T = -F_x/(0.5\rho U_\infty^2 A)$ and power coefficient $C_{Pin} = P_{in}/(0.5\rho U_\infty^3 A)$, where F_x is the streamwise component of $\boldsymbol{F}$. Note that the thrust and power evolve quickly into a periodic state after the plate begins flapping, indicating that the local dynamic processes and vortical structures in the near region of the plate dominate its force and power. Figure 6(*b*) shows the profiles of C_T and C_{Pin} during a half-cycle after the flow has reached a stationary state. We have obtained that C_T and C_{Pin} calculated by (3.4) with different analysis domains agree well with the standard stress integral (3.1). Thus, it is verified that the results are independent of the size of the analysis domain.

Consequently, we use (3.4) to reveal the relation of each vortical structure to the thrust and power. From $t/T = 0$ to 0.5, the vortical structure $R1$ is gradually generated on the plate and $R2$ is shedding into the wake. In this process, $R1$ and $R2$ usually

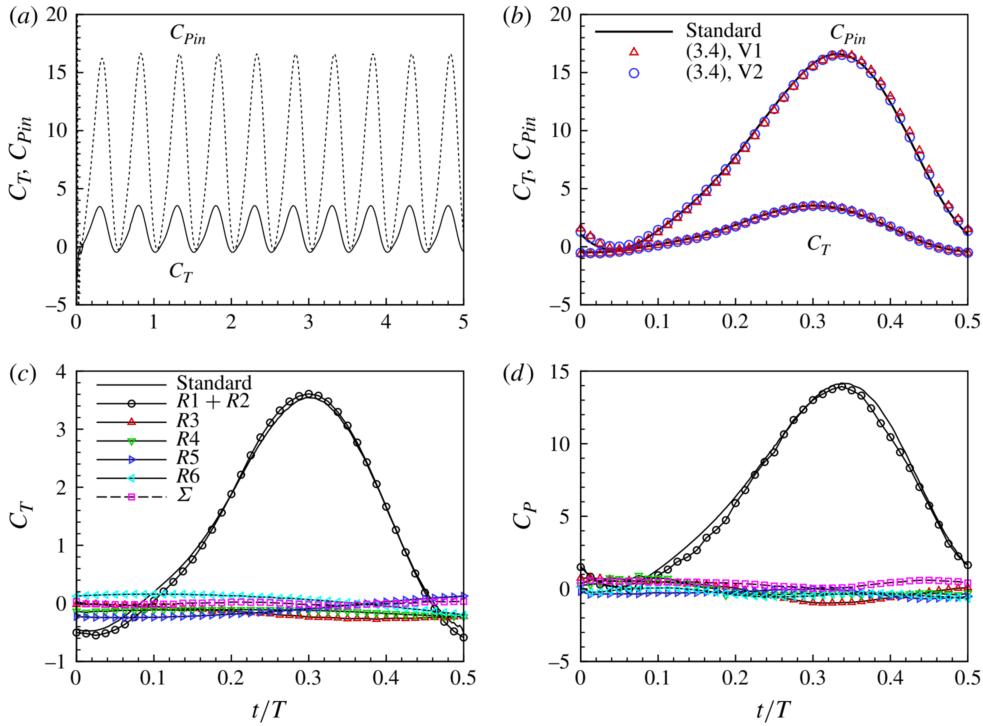

FIGURE 6. (Colour online) Thrust and power coefficients for case 1: (*a*) time-dependent thrust and power coefficients; (*b*) thrust and power calculated by the standard formulae (3.1) and (3.2) and by the dynamic expression (3.4) with different analysis domains, V1 = $[-0.6, 1.2] \times [-1, 1] \times [-0.5, 0.5]$ and V2 = $[-4, 8] \times [-5, 5] \times [-2, 2]$; (*c*,*d*) profiles of force and power due to each vortical structure and the surface integral.

connect together and their coupled contribution is thus considered. As shown in figure 6(*c*,*d*) for the profiles of C_T and $C_P = P/(0.5\rho U_\infty^3 A)$, it is identified that the major part of C_T and C_P is associated with the contribution of $R1$ and $R2$, while the other vortical structures in the wake only account for a small portion, which has been determined to be less than 5 % of the mean value of C_T and C_P. Similar force behaviour has been found by numerical solution of circular cylinder flows (Wu *et al.* 2007) and by theoretical analysis of the flapping flight model (Wang & Wu 2010). We need to indicate that the force and power contributed by $R1$ and $R2$ also contain evidently the full induced effect of the other structures in the wake. Essentially, the force and power can be well picked up by the local flow structures close to the body.

We further investigate the streamwise vortical impulse I_{xi}, which represents the streamwise component of $\boldsymbol{I}_i$, and the kinetic energy K_i of each isolated vortical structure in the wake. Here $\boldsymbol{I}_i$ and K_i are defined as

$$\boldsymbol{I}_i = \frac{\rho}{2}\int_{Ri} \boldsymbol{x} \times \boldsymbol{\omega}\, \mathrm{d}V, \quad K_i = \rho \int_{Ri} \boldsymbol{x} \cdot \boldsymbol{l}\, \mathrm{d}V, \tag{4.1}$$

where Ri represents the sub-region marked in figure 5(*c*). Then, the evolution of I_{xi} and K_i of each vortical structure is shown in figure 7. For comparison, the streamwise component of momentum M_x and the energy E of the plate transferred to the flow during a half-period or for the formation of each vortical structure are also shown in

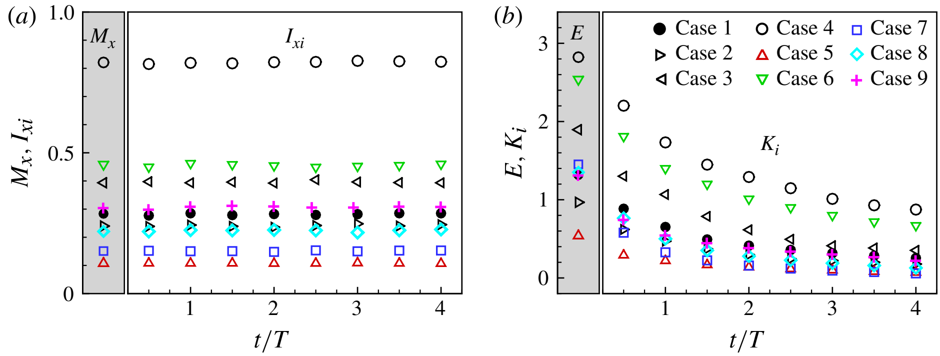

FIGURE 7. (Colour online) Time history of: (*a*) the streamwise component of the vortical impulse I_{xi}; and (*b*) the kinetic energy K_i of the vortical structure. The symbols in the grey areas represent the values of M_x and E calculated by the thrust and power of the plate. The legend from 'case 1' to 'case 9' in panel (*b*) corresponds to the cases listed in table 1.

Case	$\bar{C}_T$	η	M_x	E	Γ_0	a_0	α (deg.)	E^*	$\bar{C}_T^a$	η^a
1	1.361	0.18	0.284	1.316	1.71	0.44	74	1.02	1.38	0.18
2	1.151	0.23	0.240	0.968	1.50	0.44	74	0.97	1.21	0.20
3	1.889	0.17	0.394	1.896	2.04	0.44	73	1.04	1.74	0.17
4	1.970	0.23	0.821	2.823	2.16	0.61	70	0.99	2.07	0.23
5	0.343	0.16	0.107	0.539	1.14	0.41	80	1.01	0.33	0.16
6	2.937	0.16	0.459	2.539	2.40	0.44	73	1.00	2.73	0.14
7	0.725	0.09	0.151	1.453	1.79	0.44	82	1.03	0.73	0.10
8	1.059	0.14	0.221	1.351	1.73	0.44	77	1.03	1.14	0.15
9	1.489	0.19	0.310	1.334	1.71	0.44	71	1.04	1.62	0.21

TABLE 2. Parameters of the plate and the ring-like vortical structure. Here $\bar{C}_T$ is the mean thrust and $\eta = \bar{C}_T/\bar{C}_{Pin} = 1/(1 + \bar{C}_P/\bar{C}_T)$ is the propulsion efficiency, with $\bar{C}_{Pin}$ and $\bar{C}_P$ being the mean powers; M_x and E represent the streamwise component of momentum and the energy of the plate transferred to the flow in a half-period, respectively; Γ_0, α and a_0 are the vortex-ring parameters determined based on the flow field; E^* is described in (5.2); and $\bar{C}_T^a$ and η^a are calculated by (5.5).

figure 7 and given in table 2, and they are defined as

$$M_x = -\int_0^{T/2} F_x \,\mathrm{d}t, \quad E = \int_0^{T/2} P \,\mathrm{d}t. \tag{4.2}$$

From figure 7(*a*), I_{xi} reaches M_x at an initial stage, corresponding to evolving quickly into the periodic state in figure 6(*a*), and is nearly unchanged for $t/T \geqslant 0.5$, consistent with the small force contribution of the structures in the downstream wake in figure 6(*c*). In addition, the components of the integral vorticity of each isolated vortical structure $\int_{Ri} \boldsymbol{\omega} \,\mathrm{d}V$ are also examined and nearly vanish. These characters show that the mutual interactions of the vortical structures in the wake may be negligibly weak.

Energy dissipation always occurs due to the viscous effect during the vortex generation from the plate and the vortex evolution in the wake. Thus K_i in figure 7(*b*) decays with time, in particular within the initial period. Thus, K_i is always less than the energy of the plate transferred to the flow E. Usually, this dissipation is hardly measured. Therefore, inviscid vortex-ring models have often been used to simplify the analysis of the vortical structures in the wake of biological locomotion (e.g. Müller *et al.* 1997; Nauen & Lauder 2002; Wang & Wu 2010). As is well known, the viscous effect plays an important role in the formation and evolution of vortices and must be considered by a more realistic vortex-ring model in the dynamic analysis.

5. Analysis of dynamics based on viscous vortex-ring model

Based on the analysis of the viscous circular vortex ring (Saffman 1970), the magnitude of the vortical impulse is given by $I_v = \rho\pi\Gamma_0 a_0^2$, where Γ_0 and a_0 are the initial circulation and the initial radius of the vortex ring. Suppose that the vorticity is initially concentrated in a torus of infinitely thin core and the vorticity in the vortex core subsequently has a Gaussian distribution. The kinetic energy in the initial stage decays as (Fukumoto & Kaplanski 2008)

$$K_v \approx \frac{1}{2}\rho\Gamma_0^2 a_0 \left[\ln\left(\frac{4a_0}{\sqrt{\nu t}}\right) - C + 0.75\frac{\nu t}{a_0^2} + 0.4688\left(\frac{\nu t}{a_0^2}\right)^2\right], \tag{5.1}$$

where $C = 2.058$ is related to the Gaussian distribution across the vortex core.

We here use (5.1) to analyse the present numerical solutions of the flapping plates. The circulation Γ_0, radius a_0 and inclination angle α can be estimated from the vorticity distribution field in the cross-sectional plane as widely done in previous studies (e.g. Müller *et al.* 1997; Gharib, Rambod & Shariff 1998; Nauen & Lauder 2002). As typically shown in figure 5(d), the newly shed vortex $R2$ is used to evaluate the initial state of the equivalent vortex ring, because the circulation and radius of the viscous vortex ring remain nearly unchanged when $\nu t \ll a_0^2$. Similarly, the parameters of the initial vortex ring for the other cases are also obtained and given in table 2.

The characteristic parameters of a viscous vortex ring are used to renormalize the time and energies,

$$t^* = \frac{\nu t}{a_0^2}, \quad E^* = \frac{E}{\rho\Gamma_0^2 a_0}, \quad K_i^* = \frac{K_i}{\rho\Gamma_0^2 a_0}. \tag{5.2}$$

Then, the rescaled energy E^* can be calculated for all the cases, which are listed in table 2 and plotted in figure 8. In the analysis of the viscous vortex ring (Saffman 1970), the lower-order expression, i.e. the first two terms in (5.1), has been reasonably applied to describe different vortex rings by changing the value of C. Similarly, it is seen from figure 8 that the profiles of the rescaled kinetic energy K_v^* by (5.1) with certain values of C are well consistent with the present calculated results of K_i^*, even though the vortical structures in the wake of the flapping plate are more complicated. To understand this character, we could consider that the various factors relevant to the formation of the vortical structures may be reasonably assumed to be lumped together and be simply modelled by an adjustable parameter C.

We notice that from table 2 the rescaled energy has $E^* \approx 1$. This means that, if the magnitude of the vortical impulse is $I = \rho\pi\Gamma_0 a_0^2$ for a ring-like vortical structure as formed in the wake of the plate, the energy for the formation of this structure has $E \approx \rho\Gamma_0^2 a_0$. The relevant physical process may be clearly explained through a vortex-ring generation by impulsive motion of a circular disc in a viscous fluid (Taylor 1953), in which a plane disc-like vortex sheet is generated on the disc surface and finally rolls

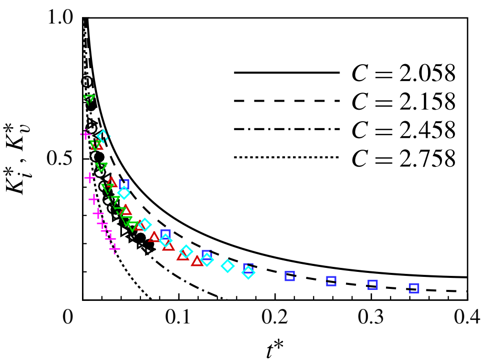

FIGURE 8. (Colour online) Rescaled kinetic energy of the ring-like vortices versus the rescaled time for all the cases in table 1. Lines and symbols represent K_v^* and K_i^*, respectively. The symbols have the same notation as in figure 7.

up to form a vortex ring. As indicated by Taylor (1953), in the beginning of the disc motion when separation of flow from the disc edge has not yet developed, the flow generated by the disc may be assumed to be potential. Thus, the initial circulation, the vortical impulse and the energy of the vortex sheet, which also represents the energy of the disc transferred to the flow, are given by

$$\Gamma_0 = \frac{4U_d a_d}{\pi}, \quad I = \frac{8}{3}\rho U_d a_d^3, \quad E = \frac{4}{3}\rho U_d^2 a_d^3, \tag{5.3}$$

where U_d is the axial velocity of disc motion and a_d is the disc radius. As Taylor (1953) indicated that the rolling up of the vortex sheet does not change the impulse and the circulation around the core, i.e. $(8/3)\rho U_d a_d^3 = \rho\pi\Gamma_0 a_0^2$, then we have $a_0 = \sqrt{2/3}\,a_d$ and the energy E^* is

$$E^* = \frac{4}{3}U_d^2 a_d^3/\Gamma_0^2 a_0 = \frac{\pi^2}{12}\sqrt{3/2} \approx 1.007, \tag{5.4}$$

which is fully consistent with our finding of $E^* \approx 1$.

Furthermore, Lighthill (1986) indicated that an accelerating body must be dressed in an acyclic attached vortex layer. Wu *et al.* (2006) then proposed the relevant mathematical formulae to describe the vortical impulse and energy, which are only dependent on the body shape and the velocity on the body surface. Additionally, in the unsteady wing theory for animal locomotion, the vortex layer on the body surface can be simplified as formed by a series of vortex lines, with each line forming a closed loop, and these loops result in the formation of the ring-like vortices in the wake (Wu 2011). For the flapping plate considered here, even though the generation and evolution of the planar vortex sheet on the plate surface become more complex, the vortices will mainly form the ring-like structures as typically shown in figure 5 and then $E^* \approx 1$ holds well.

From the preceding analysis, since the vortical impulse $\boldsymbol{I}_i$ is always close to the momentum $\boldsymbol{M}$ and the energy E^* is close to 1, the formulae for thrust and efficiency can be approximately obtained solely in terms of the equivalent vortex-ring parameters of the ring-like vortical structure:

$$\bar{T}^a = \frac{I_x}{T/2} = 2\rho\pi\Gamma_0 a_0^2\cos\alpha/T, \quad \eta^a = 1\bigg/\left(1 + \frac{\Gamma_0}{\pi a_0 U_\infty \cos\alpha}\right). \tag{5.5}$$

Then, the thrust coefficient $\bar{C}_T^a = \bar{T}^a/(0.5\rho U_\infty^2 A)$ and efficiency η^a predicted by (5.5) are given in table 2, which are consistent with the numerical results. Moreover, using (5.5) we can qualitatively analyse the propulsive performance in terms of the topology of a ring-like vortical structure. A vortex ring with larger Γ_0, larger a_0 or smaller inclination angle α will generate larger thrust on the body, while a vortex ring with smaller Γ_0 corresponds to higher efficiency. Also a vortex ring with larger radius is more favourable for locomotion.

We further apply (5.5) to deal with efficiency in biological locomotion. The prediction is based on the measurement of the mean morphological parameters and the wake vortices of mullet (*Chelon labrosus*) by Müller *et al.* (1997), including mean swimming speed of approximately $U_\infty = 0.175$ m s^{-1}, mean ring radius $a_0 = 0.019$ m, circulation $\Gamma_0 = 7.6 \times 10^{-4}$ m^2 s^{-1} and inclination angle $\alpha = 40^\circ$. We then employ (5.5) to obtain an efficiency of around 91 %. For comparison, Müller *et al.* (1997) also used an inviscid vortex-ring model to predict an efficiency around 97 %. The difference between the two values is apparently related to the use of the viscous and inviscid vortex-ring models and is essentially associated with energy dissipation as discussed above. Furthermore, considering another experiment on chub mackerel (*Scomber japonicus*) by Nauen & Lauder (2002), the measured parameters are described as follows: two swimming speeds of 1.2 and 2.2 fork lengths per second, i.e. 26.4–31.2 cm s^{-1} and 48.4–57.2 cm s^{-1} in terms of several fork lengths used in the experiment, corresponding mean radii of the ring 0.82 and 0.93 cm, mean circulations 31 and 52 cm^2 s^{-1} and inclination angles 56 and 63°. Then the efficiency is calculated by (5.5) to be 82–90 %, lying in the range adopted by animal locomotion (Wu 2011).

The robustness of (5.5) is examined for sensitivity to measurement inaccuracy of α, Γ_0 and a_0. Based on extensive measurements (e.g. Müller *et al.* 1997; Gharib *et al.* 1998; Drucker & Lauder 1999; Nauen & Lauder 2002), we assume that the inaccuracy in the calculation of α, Γ_0 and a_0 by the vorticity distribution measured by digital particle image velocimetry is 5 %, and the average inclination angle of the vortex ring produced in bio-locomotion is $\sim$50°. Then the deviations of thrust and efficiency predicted by (5.5) are around 5 and 1 %, respectively, indicating that the formulae should be insensitive to the inevitable measurement inaccuracy, in particular for the efficiency.

From the above analysis, the formation of a ring-like vortical structure from a planar vortex sheet reasonably possesses the relation $E^* \approx 1$. Here we briefly analyse this relation for the general situation by means of theoretical vortex-ring models and experimental measurements. Norbury (1973) proposed a family of steady vortex rings, in which the ratio of the core radius and the ring radius ε_0 ranges from 0 (circular line vortex) to $\sqrt{2}$ (Hill's vortex), with kinetic energy from $K^* \rightarrow \infty$ to $K^* \approx 0.284$, respectively. Some experimental investigations were carried out for the dynamics of thin vortex rings (Sullivan *et al.* 2008) and the formation of thick vortex rings (Gharib *et al.* 1998). From the experimental data, we can reasonably obtain $E^* \sim O(1)$. Furthermore, based on the measurements of animal locomotion (e.g. Müller *et al.* 1997; Nauen & Lauder 2002), the ring-like vortical structures in the nearest wake have $\varepsilon_0 \sim 0.3$ and then $E^* \approx 1$ is also well estimated, consistent with the present prediction in terms of the numerical results.

6. Concluding remarks

The dynamics of a flapping plate and the connections with local dynamic processes and vortical structures are investigated. Various fundamental mechanisms dictating the flapping locomotion are briefly summarized as follows. The force and power of the flapping plate are strongly dominated by the flow structures close to the body. The vortical impulse of each individual vortical structure almost remains unchanged and is close to the momentum of the plate transferred to the flow for the formation of this vortical structure, while the kinetic energy decays and is always less than the energy of its formation. The evolution of the kinetic energy of the vortical structure in the wake is essentially consistent with the viscous vortex-ring model, and the rescaled energy E^* of the plate transferred to the flow is around 1, which also confirms the finding of the vortex-ring generation by impulsive motion of a circular disc (Taylor 1953). Furthermore, simplified formulae for thrust and efficiency can be reasonably proposed, which have been verified to be reliable by numerical solutions and experimental measurements of animal locomotion.

Acknowledgements

The authors are very grateful to Professor J.-Z. Wu for valuable discussions. This work was supported by the Natural Science Foundation of China (Grant 10832010), the Innovation Project of the Chinese Academy of Sciences (Grant KJCX2-YW-L05) and the 111 Project (Grant B07033).

REFERENCES

ALTSHULER, D. L., PRINCEVAC, M., PAN, H. & LOZANO, J. 2009 Wake patterns of the wings and tail of hovering hummingbirds. *Exp. Fluids* **46**, 835–846.

BLONDEAUX, P., FORNARELLI, F., GUGLIELMINI, L., TRIANTAFYLLOU, M. S. & VERZICCO, R. 2005 Numerical experiments on flapping foils mimicking fish-like locomotion. *Phys. Fluids* **17**, 113601.

BUCHHOLZ, J. H. J. & SMITS, A. J. 2008 The wake structure and thrust performance of a rigid low-aspect-ratio pitching panel. *J. Fluid Mech.* **603**, 331–365.

CHANG, C. C. 1992 Potential flow and forces for incompressible viscous flow. *Proc. R. Soc.* A **437**, 517–525.

CHEN, S. & DOOLEN, G. D. 1998 Lattice Boltzmann method for fluid flows. *Annu. Rev. Fluid Mech.* **30**, 329–364.

DABIRI, J. O. 2009 Optimal vortex formation as a unifying principle in biological propulsion. *Annu. Rev. Fluid Mech.* **41**, 17–33.

DAI, H., LUO, H. X. & DOYLE, J. F. 2012 Dynamic pitching of an elastic rectangular wing in hovering motion. *J. Fluid Mech.* **693**, 473–499.

DICKINSON, M. H., LEHMANN, F.-O. & SANE, S. P. 1999 Wing rotation and the aerodynamic basis of insect flight. *Science* **284**, 1954.

DICKSON, W. B. & DICKINSON, M. H. 2004 The effect of advance ratio on the aerodynamics of revolving wings. *J. Expl Biol.* **207**, 4269–4281.

DONG, H., MITTAL, R. & NAJJAR, F. M. 2006 Wake topology and hydrodynamic performance of low-aspect-ratio flapping foils. *J. Fluid Mech.* **566**, 309–343.

DRUCKER, E. G. & LAUDER, G. V. 1999 Locomotor forces on a swimming fish: three-dimensional vortex wake dynamics quantified using particle image velocimetry. *J. Expl Biol.* **202**, 2393–2412.

VON ELLENRIEDER, K. D., PARKER, K. & SORIA, J. 2003 Flow structures behind a heaving and pitching finite-span wing. *J. Fluid Mech.* **490**, 129–138.

ELLINGTON, C. P. 1984*a* The aerodynamics of hovering insect flight. II. Morphological parameters. *Phil. Trans. R. Soc. Lond.* B **305**, 17–40.

ELLINGTON, C. P. 1984*b* The aerodynamics of hovering insect flight. III. Kinematics. *Phil. Trans. R. Soc. Lond.* B **305**, 41–78.

FENG, Z.-G. & MICHAELIDES, E. E. 2004 The immersed boundary–lattice Boltzmann method for solving fluid–particles interaction problems. *J. Comput. Phys.* **195**, 602–628.

FILIPPOVA, O. & HÄNEL, D. 1998 Grid refinement for lattice–BGK models. *J. Comput. Phys.* **147**, 219–228.

FUKUMOTO, Y. & KAPLANSKI, F. 2008 Global time evolution of an axisymmetric vortex ring at low Reynolds numbers. *Phys. Fluids* **20**, 053103.

GAO, T. & LU, X.-Y. 2008 Insect normal hovering flight in ground effect. *Phys. Fluids* **20**, 087101.

GHARIB, M., RAMBOD, E. & SHARIFF, K. 1998 A universal time scale for vortex ring formation. *J. Fluid Mech.* **360**, 121–140.

GOLDSTEIN, D., HANDLER, R. & SIROVICH, L. 1993 Modeling a no-slip flow boundary with an external force field. *J. Comput. Phys.* **105**, 354–366.

HEDENSTRÖM, A., JOHANSSON, L. C., WOLF, M., VON BUSSE, R., WINTER, Y. & SPEDDING, G. R. 2007 Bat flight generates complex aerodynamic tracks. *Science* **316**, 894–897.

HEDENSTRÖM, A., ROSÉN, M. & SPEDDING, G. R. 2006 Vortex wakes generated by robins *Erithacus rubecula* during free flight in a wind tunnel. *J. R. Soc. Interface* **3**, 263–276.

HSIEH, C. T., CHANG, C. C. & CHU, C. C. 2009 Revisiting the aerodynamics of hovering flight using simple models. *J. Fluid Mech.* **623**, 121–148.

HSIEH, C. T., KUNG, C. F., CHANG, C. C. & CHU, C. C. 2010 Unsteady aerodynamics of dragonfly using a simple wing–wing model from the perspective of a force decomposition. *J. Fluid Mech.* **663**, 233–252.

HUNT, J. C. R., WRAY, A. A. & MOIN, P. 1988 Eddies, stream, and convergence zones in turbulent flows. *Tech. Rep.* CTR-S88. Center for Turbulence Research, 193-208.

LI, G.-J., ZHU, L. & LU, X.-Y. 2012 Numerical studies on locomotion performance of fish-like tail fins. *J. Hydrodyn.* B **24**, 488–495.

LIGHTHILL, M. J. 1986 *An Informal Introduction of Theoretical Fluid Mechanics*. Clarendon.

MÜLLER, U. K., VAN DEN HEUVEL, B. L. E., STAMHUIS, E. J. & VIDELER, J. J. 1997 Fish foot prints: morphology and energetics of the wake behind a continuously swimming mullet (*Chelon labrosus* Risso). *J. Expl Biol.* **200**, 2893–2906.

NARASIMHAN, M., DONG, H. B., MITTAL, R. & SINGH, S. N. 2006 Optimal yaw regulation and trajectory control of biorobotic AUV using mechanical fins based on CFD parametrization. *Trans. ASME: J. Fluids Engng* **128**, 687–698.

NAUEN, J. C. & LAUDER, G. V. 2002 Hydrodynamics of caudal fin locomotion by chub mackerel, *Scomber japonicus* (Scombridae). *J. Expl Biol.* **205**, 1709–1724.

NORBURY, J. 1973 A family of steady vortex rings. *J. Fluid Mech.* **57**, 417–431.

PESKIN, C. S. 2002 The immersed boundary method. *Acta Numerica* **11**, 479–517.

RICHARD, B. 1958 The speed of swimming of fish as related to size and to the frequency and amplitude of the tail beat. *J. Expl Biol.* **35**, 109–133.

SAFFMAN, P. G. 1970 The velocity of viscous vortex rings. *SIAM J.* **49**, 371–380.

SAMBILAY, V. C. 1990 Interrelationships between swimming speed, caudal fin aspect ratio and body length of fishes. *ICLARM Fishbyte* **8**, 16–20.

SHI, X. & LIM, S. P. 2007 A LBM-DLM/FD method for 3D fluid–structure interactions. *J. Comput. Phys.* **226**, 2028–2043.

SULLIVAN, I. S., NIEMELA, J. J., HERSHBERGER, R. E., BOLSTER, D. & DONNELLY, R. J. 2008 Dynamics of thin vortex rings. *J. Fluid Mech.* **609**, 319–347.

TAIRA, K. & COLONIUS, T. 2009 Three-dimensional flows around low-aspect-ratio flat-plate wings at low Reynolds numbers. *J. Fluid Mech.* **623**, 187–207.

TAYLOR, G. I. 1953 Formation of a vortex ring by giving an impulse to a circular disk and then dissolving it away. *J. Appl. Phys.* **24**, 104.

TAYLOR, G., NUDDS, R. & THOMAS, A. 2003 Flying and swimming animals cruise at a Strouhal number tuned for high power efficiency. *Nature* **425**, 707–711.

WANG, X. X. & WU, Z. N. 2010 Stroke-averaged lift forces due to vortex rings and their mutual interactions for a flapping flight model. *J. Fluid Mech.* **654**, 453–472.

WILLMOTT, A. P., ELLINGTON, C. P. & THOMAS, A. L. R. 1997 Flow visualization and unsteady aerodynamics in the flight of the hawkmoth, *Manduca sexta*. *Phil. Trans. R. Soc. Lond.* B **352**, 303–316.

WITHERS, P. C. 1981 An aerodynamic analysis of bird wings as fixed aerofoils. *J. Expl Biol.* **90**, 143–162.

WU, J.-C. 1981 Theory for aerodynamic force and moment in viscous flow. *AIAA J.* **19**, 432–441.

WU, J.-Z., LU, X.-Y. & ZHUANG, L.-X. 2007 Integral force acting on a body due to local flow structures. *J. Fluid Mech.* **576**, 265–286.

WU, J.-Z., MA, H.-Y. & ZHOU, M.-D. 2006 *Vorticity and Vortex Dynamics*. Springer.

WU, T. Y. 2011 Fish swimming and bird/insect flight. *Annu. Rev. Fluid Mech.* **43**, 25–58.

XU, C.-Y., CHEN, L.-W. & LU, X.-Y. 2010 Large-eddy simulation of the compressible flow past a wavy cylinder. *J. Fluid Mech.* **665**, 238–273.

YU, D. Z., MEI, R. W. & SHYY, W. 2002 A multi-block lattice Boltzmann method for viscous fluid flows. *Intl J. Numer. Meth. Fluids* **39**, 99–120.

ZHANG, J., LIU, N.-S. & LU, X.-Y. 2010 Locomotion of a passively flapping flat plate. *J. Fluid Mech.* **659**, 43–68.